The Equatorial Thermocline Outcropping—A Seasonal Control on the Tropical Pacific Ocean–Atmosphere Instability Strength

ELI GALANTI AND ELI TZIPERMAN

Environmental Sciences, Weizmann Institute, Rehovot, Israel

MATTHEW HARRISON AND ANTONY ROSATI

NOAA/GFDL, Princeton, New Jersey

RALF GIERING

FastOpt, Hamburg, Germany

ZIV SIRKES

Institute of Marine Science, University of Southern Mississippi, Stennis Space Center, Mississippi

(Manuscript received 7 August 2001, in final form 3 April 2002)

ABSTRACT

One of the major factors determining the strength and extent of ENSO events is the instability state of the equatorial Pacific coupled ocean–atmosphere system and its seasonal variations. This study analyzes the coupled instability in a hybrid coupled model of the Indo–Pacific region, using the adjoint method for sensitivity studies.

It is found that the seasonal changes in the ocean–atmosphere instability strength in the model used here are related to the outcropping of the thermocline in the east equatorial Pacific. From July to December, when the thermocline outcrops over a wide area in the east Pacific, there is a strong surface–thermocline connection and anomalies that arrive as Kelvin waves from the west along the thermocline can reach the surface and affect the SST and thus the coupled system. Conversely, from February to June, when the thermocline outcropping is minimal, the surface decouples from the thermocline and temperature anomalies in the thermocline depth range do not affect the surface and dissipate within the thermocline. The role of vertical mixing rather than upwelling in linking vertical thermocline movements to SST changes is emphasized.

It is therefore suggested that the seasonal ocean–atmosphere instability strength in the equatorial Pacific is strongly influenced by the thermocline outcropping and its seasonal modulation, a physical mechanism that is often neglected in intermediate coupled models and that can be represented properly only in models that employ the full dynamics of the mixed layer.

1. Introduction

One of the major factors determining the strength and extent of ENSO events, is the instability state of the equatorial Pacific ocean–atmosphere system. This instability is determined to a large degree by the ocean–atmosphere ''coupling strength'' (Cane et al. 1990), so that the instability strength and the coupling strength may be considered alternative measures of the same physical quantity. An unstable state allows the growth of anomalous conditions that can then evolve to become an El Niño event, whereas a stable state causes any perturbation to vanish, forcing the system to stay at its mean seasonal state.

The instability strength in the equatorial Pacific region undergoes seasonal variations (e.g., Philander 1983; Hirst 1986; Battisti and Hirst 1989), along with variations whose timescale range from few years to decades (e.g., Gu and Philander 1995, 1997). Understanding the physical factors determining the strength and the seasonal variability of the coupled instability is an important task because it has implications for both El Niño's predictability (Webster and Yang 1992; Torrence and Webster 1998; Weiss and Weiss 1999; Xue et al. 1994; Chen et al. 1995; Moore and Kleeman 1996), as well as for ENSO's irregularity (Tziperman et al. 1994, 1995; Jin et al. 1994; Chang et al. 1994) and phase locking (Tziperman et al. 1998; Galanti and Tziperman 2000).

Corresponding author address: Dr. Eli Galanti, Dept. of Environmental Sciences, Weizmann Institute of Science, Rehovot 76100, Israel.
E-mail: eli.galanti@weizmann.ac.il

Philander (1983) suggested that the key element determining the seasonality of the coupled instability strength is the seasonal movement of the Pacific intertropical convergence zone (ITCZ) and its effect on the atmospheric heating. Other seasonal climatological factors that might enhance the coupled ocean–atmosphere instability are large zonal gradients of mean SST, shallow thermocline, strong zonal winds, high SST (Hirst 1986) and strong upwelling (Battisti 1988). Battisti and Hirst (1989) found that setting the basic state in a simplified model to different monthly climatologies affects the rate of anomaly growth. Analyzing separately the effect of each seasonal variable in an intermediate model, Tziperman et al. (1997) suggested that the seasonal wind convergence (i.e., the ITCZ location) and the seasonal climatological SST are the dominant factors in determining the strength of the ocean–atmosphere instability in the Cane–Zebiak (CZ) model (Zebiak and Cane 1987). All the above works used simplified models, ranging from low-order models to intermediate models (such as the CZ model), which lack the ability to explicitly resolve the mixed layer and the thermocline structure.

In this paper we suggest an additional mechanism for the seasonality in the coupled instability strength. We emphasize the role of vertical mixing between the thermocline and the sea surface and show that seasonal changes in the strength of the SST response to thermocline movements is a function of the extent of outcropping of the thermocline in the east equatorial Pacific. That is, we show that from summer to early winter when the thermocline outcrops over a wide area in the east Pacific, there is a strong surface–thermocline connection and anomalies that arrive as Kelvin waves from the west along the thermocline can reach the surface and affect the SST and thus the coupled system. Conversely, from late winter to early spring, when the thermocline outcropping is minimal, the surface decouples from the thermocline and temperature anomalies in the thermocline depth range do not affect the surface and dissipate within the thermocline. We therefore suggest that the seasonal ocean–atmosphere coupling strength is strongly influenced by the seasonality in the thermocline outcropping in the east Pacific.

The results of this work were obtained using the adjoint method for sensitivity studies (e.g., Hall 1986; Errico and Vukicevic 1992; Moore and Kleeman 1996, 1997; Giering 1997; Giering and Kaminski 1998; Marotzke et al. 1999; Sirkes and Tziperman 2001; van Oldenborgh et al. 1999; van Oldenborgh 2000). The adjoint method was applied to a hybrid coupled model of the Indo-Pacific region, that is based on an ocean general circulation model (GCM) coupled to a statistical atmospheric model (e.g., Syu et al. 1995). Our results regarding the physics of ENSO, however, do not depend on the particular methodology of sensitivity analysis used here. We have made an effort to present the work in a way that would hopefully be clear to readers with no previous exposure to the adjoint method.

The sensitivity analysis in this paper is arranged and presented as follows. We first describe the hybrid coupled ENSO model, along with the adjoint model that was constructed for the sensitivity studies (section 2), and the design of the sensitivity experiments is presented in section 3. The actual sensitivity analysis begins with section 4, in which we examine the sensitivity of the averaged subsurface thermocline-depth temperature in the east Pacific to processes in the entire equatorial Pacific in an ocean-only model. We show that the east Pacific subsurface temperature is sensitive to the thermocline-depth temperature to the west, due to the Kelvin waves that can transmit the signal from the west Pacific to the east Pacific. The purpose of this section is to introduce the reader to the adjoint analysis and to looking at the adjoint model results. Next, in section 5, we consider the sensitivity of the same averaged temperature in the subsurface east Pacific, but in a coupled model. We show that in this case, the sensitivity increases in time, indicating that the coupled ocean–atmosphere amplifies temperature anomalies because of its instability, which is responsible for ENSO's development in our model. The coupled instability acts as follows: subsurface east Pacific temperature anomalies are transmitted to the surface, affect the east Pacific SST and therefore the wind stress in the central Pacific. The wind stress then creates a temperature signal along the thermocline in the central Pacific, which is transmitted to the east Pacific as Kelvin waves and amplifies the original signal there. Now, there are two issues to note here: first, the fact that we observe an amplification by the coupled system means that there is a connection between the subsurface and surface temperatures in the east Pacific. This connection is our focus here and is further explored in the following. Second, the instability or amplification by the coupled ocean–atmosphere system is seen here via the adjoint analysis, and we would like to spend a few lines explaining this.

Consider the system

$$\frac{dx}{dt} = \alpha x, \tag{1}$$

where x is a scalar variable, and α is a constant coefficient. Suppose the cost function (the scalar quantity whose sensitivity we are after) is simply some constant β times the model variable x at the final time T

$$J = \beta x(T). \tag{2}$$

The adjoint equation in this case can be shown to be (e.g., Tziperman and Thacker 1989; Thacker 1987)

$$\frac{d\lambda}{dt} = -\alpha\lambda + \beta\delta(t - T), \tag{3}$$

where $\delta(t - T)$ is the Dirac delta function. Note that the adjoint equation starts with zero initial conditions

at time T, $\lambda(t = T) = 0$, is then forced by the cost function value at that time, and is integrated backward in time, from time T to the initial time $t = 0$. Given that the adjoint equation for $\lambda(t)$ is integrated backward in time, its behavior is exactly the same as that of the forward equation: if α is positive, that is, the model is unstable and x is growing in time, then the adjoint solution λ will also grow backward in time. The behavior of the adjoint solution is therefore a direct measure of the model instability. An adjoint solution that grows backward in time indicates that the model is unstable with regard to the chosen cost function, whereas an adjoint solution that decays backward in time indicates that the model is stable. We will take advantage of this when analyzing the adjoint solution of the coupled model, and examining its stability.

Having observed the coupled instability via the subsurface to surface connection, we next (section 6) examine the same sensitivity of the subsurface east Pacific temperature during a different month, when the thermocline does not outcrop in the east Pacific. We find that in this case the adjoint solution grows less rapidly backward in time, indicating that the forward model is less unstable. We conclude that the subsurface to surface connection in the east Pacific is less strong, because the thermocline does not outcrop, and as a result the coupled instability is weaker. Finally, in section 7, we examine the sensitivity of the SST in the east Pacific to the subsurface temperature, and explicitly examine the role of vertical mixing in order to demonstrate that the seasonality of the thermocline outcropping indeed affects the seasonality in the ocean–atmosphere coupling strength and coupled instability. We conclude in section 8.

2. The hybrid coupled model

The hybrid coupled model we use is constructed from an ocean GCM coupled to a monthly statistical atmosphere. In the following sections we describe the different components of the hybrid coupled model.

a. The ocean model

The ocean model is based on the Geophysical Fluid Dynamics Laboratory (GFDL) modular ocean model (MOM; Pacanowski and Griffies 1999). The model domain is the Indo–Pacific region, 50°S–50°N, and 30°E–70°W. The model resolution is 3° in longitude, 3° going to 1° at the equator in latitude, and 30 depth levels where the top 15 layers are within the top 200 m of the ocean. The resolution is such that the equatorial dynamics (Kelvin and Rossby waves) are resolved (with a Rossby radius of deformation being roughly 250 km, there are some five grid points in latitude to marginally represent the Kelvin wave structure in latitude over both sides of the equator), while the number of grid points is still small enough to enable many long model runs.

The model uses a modified Richardson number–dependent vertical mixing scheme (Pacanowski and Philander 1981; Syu and Neelin 2000). In addition, a simplified mixed layer scheme is applied as in Syu and Neelin (2000). Constant horizontal viscosity and diffusivity are used. Sponge layers are used at the north and south horizontal boundaries, restoring the temperature and salinities to the monthly Levitus climatology (Levitus 1982).

The model is spun up and forced by the climatological Florida State University (FSU) wind stress (Stricherz and Legler 1992; Legler et al. 1997) and climatological heat fluxes (Esbensen and Kushnir 1981). The model is also restored to the climatological monthly National Centers for Environmental Prediction (NCEP) SST (Reynolds and Smith 1994) and to the climatological monthly Levitus sea surface salinity (SSS; Levitus 1982) with a restoring time of 10 days (for an upper-layer thickness of 10 m). After reaching its mean seasonal climate state (50 yr of spinup), the monthly mean model air–sea heat flux is saved to be used as a flux adjustment term in the coupled run. A weak restoring of the temperature to the climatological SST of the ocean model during the spinup, with a timescale of 100 days, is applied during the coupled model run. The monthly temperature climatology of the coupled model is similar to the Levitus climatology (Levitus 1982).

b. Statistical atmospheric model

The statistical atmospheric model is based on that of Harrison et al. (2002, hereafter HAR; see also Syu et al. 1995), using the NCEP SST (Reynolds and Smith 1994), and the wind stress and heat fluxes of the European Centre for Medium-Range Weather Forecasts (ECMWF) reanalysis (Gibson et al. 1997). The atmospheric model is constructed by finding the best-correlated patterns of the two datasets (SST anomalies vs atmospheric anomalies) using a singular value decomposition (SVD) of the cross-covariance matrix of the SST and the atmospheric variables (e.g., Syu et al. 1995). The first few singular vectors are then used to predict the wind stress and heat flux anomalies based on the model SST anomalies. HAR have shown that only the first two or three singular vectors should be used; the use of higher modes could introduce an unphysical, relatively large-scale noise into the model. We chose to use the first three SVD modes. The coupling of the atmospheric variables to the anomalous SST (see details below) is done only between 20°S and 20°N. This choice was made in order to avoid spurious tropical–extratropical teleconnections that may occur due to the fact that the atmospheric model is derived from only 15 yr of data. It is known that different flux products that are used to derive statistical atmospheric models result sometimes in self-sustained and sometimes in damped variability (HAR). In this model we do not use an artificially enhanced (stronger) coupling coefficient, and the coupling is therefore not artificially

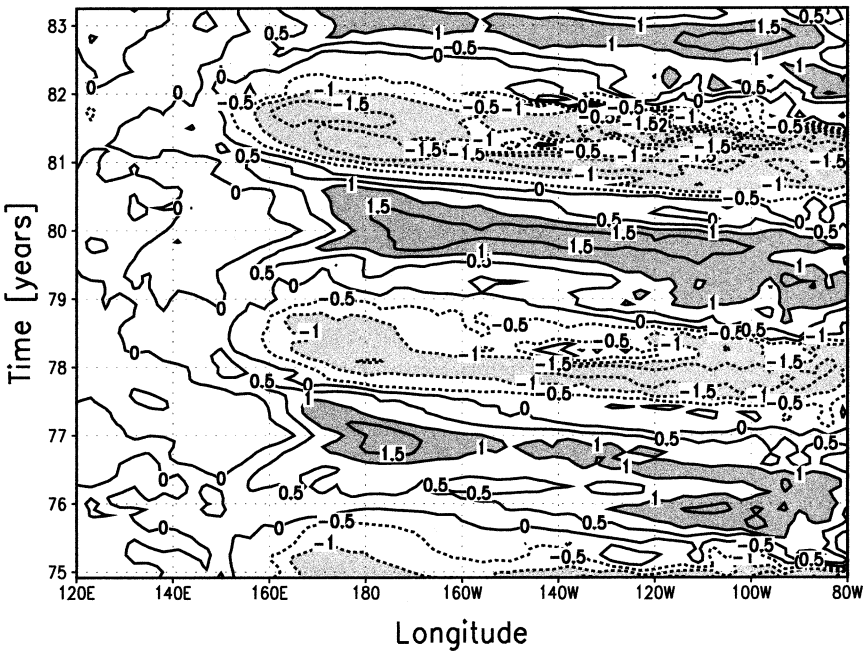

FIG. 1. The hybrid coupled model temperature anomalies along the equator, averaged from 5°S to 5°N, as a function of time (years after spinup). Values larger (smaller) than 1.0°C (−1.0°C) are shaded with dark (light) gray.

tuned to result in self-sustained oscillations. Also, we are not using (see end of section 2a) a strong restoring heat flux in addition to the heat flux calculated by the statistical atmosphere when running the coupled model. This allows for thermal anomalies to exist and evolve more freely.

Note that the resulting estimate of the atmospheric forcing fields does not account for high-frequency variability (i.e., frequencies higher than one month) and for wind stress anomalies induced by midlatitude teleconnections. Also note that the rms variability of the atmospheric anomalous response in our model will be smaller than the observed one since we exclude the energy contained in the higher SVD modes, being interested in the large-scale low-frequency dynamics.

c. The hybrid coupled model

The coupled model is run as follows: at each time step, the SST anomalies are calculated with respect to the monthly climatological SST of the uncoupled ocean model. Next, the wind stress and heat flux anomalies are derived from the SST anomalies using the statistical atmospheric model. Finally, the calculated wind stress and heat flux anomalies are added to the monthly climatological FSU wind stress and to the climatological model heat flux, respectively, to be used as forcing for the ocean model.

The model exhibits interannual variability similar to, although weaker than, the observed ENSO variability (Fig. 1). The SST anomalies are mainly in the east and central Pacific, the oscillation timescale is 3–4 yr and the maximum of the warm events is reached during November–December, in reasonable agreement with observations. Note that the model oscillations are more regular than the observed, and that the interannual variance in the central Pacific is similar to that in the eastern Pacific, while in the observations it is smaller. Also note that the La Niña events are slightly stronger than the El Niño events, which may indicate that the nonlinearity dominant in the model is not identical to that in reality.

d. The adjoint model

An adjoint model for the hybrid coupled model was derived with the help of the tangent linear and adjoint model compiler (Giering and Kaminski 1998; Giering 1997; Marotzke et al. 1999). This compiler derives an adjoint code for a given FORTRAN code, provided that the compiler can recognize all the structures and syntax of the original code.

Many changes were made to MOM to make it more consistent with the adjoint compiler. In addition, a set of PERL scripts were developed to convert structures in the MOM code that the compiler could not handle. Those include most of the FORTRAN90 code and some FORTRAN77 commands. In order to verify the adjoint code, its solution was compared at each grid point to a finite-difference estimate of the derivative of the cost function. For an appropriately small amplitude perturbation to the initial conditions, the finite-difference gra-

dient of the cost function was found to converge to the adjoint solution, up to the truncation error.

3. Sensitivity analysis methodology

Two factors determine the physical context of our sensitivity experiments: the first is the formulation of the cost function, and the second is the choice of the control variables. The cost function is the index (a scalar) whose sensitivity is studied with respect to changes in the control variables. We start this section with a brief review of the adjoint method for sensitivity studies, followed by a detailed description of the specific experiments we carried out.

a. Sensitivity studies—General formulation

Let us denote the model initial conditions by a vector $\mathbf{X}_{\text{init}}$. These initial conditions can be any combination of the model variables (temperature, salinity, currents, etc.). The initial conditions, also referred to here as ''control variables,'' are then propagated in time by the model equations, which we denote here by an operator $\mathbf{L}_\tau$, so that

$$\mathbf{X}_{\text{final}} = \mathbf{L}_\tau(\mathbf{X}_{\text{init}}), \tag{4}$$

where the vector $\mathbf{X}_{\text{final}}$ is the final state of the model, and τ is the time interval over which the model was integrated. The next stage is to define a scalar ''cost function'' from the model solution, possibly based on the solution at several time steps. The cost function is usually a measure of a model characteristic we would like to study; in our case, it will be a measure of the amplitude of ENSO. Let the cost function, as a function of the final model state, be

$$J = J(\mathbf{X}_{\text{final}}), \tag{5}$$

and since the final state depends on the initial one, we can also write

$$J = J(\mathbf{X}_{\text{init}}). \tag{6}$$

We now ask the following question: what would be the sensitivity of the cost function J to perturbation in the kth control variables x^k_{init} (note that the index k stands for different spatial locations and various physical variables such as temperature, currents, etc.). The sensitivity is simply the derivative, so that

$$\lambda^k = \frac{\partial J}{\partial x^k_{\text{init}}}, \tag{7}$$

where λ^k denotes the derivative of the cost function with respect to the kth control variable, or in other words, λ^k is the sensitivity of the cost function to the kth control variable.

To compute the sensitivity λ^k, one could run the model once without any perturbation and once with a small perturbation δx in the kth control variables, and estimate the cost function gradient by

$$\lambda^k_{\text{es}} = \frac{J(x^k_{\text{init}} = x^k_0 + \delta x) - J(x^k_{\text{init}} = x^k_0)}{\delta x}, \tag{8}$$

where λ^k_{es} is the estimated finite-difference approximation to the gradient of the cost function with respect to the kth control variable, and x^k_0 is the kth control variable without perturbation. One would then have to run the model again for each control variable in order to get the full vector of sensitivities. That is, of course, an impractical procedure when dealing with complicated 3D models with $O(10^6)$ initial conditions (control variables) such as our hybrid coupled model. The adjoint method enables us to compute all the sensitivities λ^k, $k = 1, \ldots, K$ by running the forward (physical) model once, and then its adjoint model only once (computationally equivalent to about four runs of the physical model). The adjoint model runs backward in time, from the time of the cost function evaluation to the time of the initial conditions; in other words, it propagates the sensitivity backward, from the effect to the cause. It computes not only the sensitivities to the control variables at the initial time, but also the sensitivities at all intermediate time intervals until the time at which the cost function is evaluated.

In order to obtain a feeling for the physical contents of the adjoint model solution, consider a (rigid lid) two-layer equatorial ocean model in which baroclinic Kelvin waves exist, so that any perturbation to the model variables propagates eastward as equatorial Kelvin waves. Defining the cost function to be the upper-layer depth at some location along the equator, the adjoint model solution will be the sensitivity of the upper-layer depth at the chosen location to perturbations in all model variables at previous times. Since the model allows for eastward-propagating Kelvin waves to exist, the cost function would be sensitive to Kelvin waves that were excited west of the location of the cost function, at a time interval that is exactly the time it takes the Kelvin wave to reach the location where the cost function is evaluated. The adjoint model, running backward in time, will manifest this sensitivity in the shape of an adjoint Kelvin wave that propagates westward from the location of the cost function evaluation to the distance that an actual Kelvin wave would have propagated during the same time interval.

It is important to remember that the adjoint sensitivities are based on the model tangent-linearization and therefore represent the sensitivity to infinitesimal perturbations. Any nonlinearity (such as the Richardson number vertical-mixing scheme) will affect the accuracy of the sensitivity to larger amplitude perturbations.

b. Formulation of the cost function

The cost function we use focuses on the temperature variability in the east Pacific. The largest amplitude interannual temperature variability observed in the equatorial Pacific (as well as in our model) is located near

100°W at a depth of about 60 m. Fig. 2 shows the root-mean-square (rms) of the coupled-model interannual temperature variability along the equator (averaged over 5°S–5°N). Two main features can be seen: the first is the large-amplitude variability in the east that is due to the El Niño and La Niña signal, and the second is located just beneath the warm pool due to a signal of opposite sign to that of the east Pacific SST; that feature is formed during the mature phase of the El Niño/La Niña event and is the negative feedback that later on propagates to the east and terminates the event. The Niño-3 (5°N–5°S, 90°–150°W) index is the surface manifestation of the first feature. For example, an SST anomaly at the peak time of ENSO of 3°C, corresponds to a temperature anomaly at depth of 60 m of about 9°C at 100°W (these temperature differences are true also for the observed ENSO).

As will be seen below, our sensitivity experiments mostly need to be based on a cost function that focuses on the region of largest variability. We therefore set the cost function to be a summation of temperature, weighted toward the regions of maximum rms temperature variability in the east Pacific (Fig. 2). The cost function also sums the temperature over a short time interval around a time $t_{\max}$, with a Gaussian-like weight that has a timescale of $\Delta T = 10d$ days, so that the cost function has contributions from the temperature at a range of times around $t_{\max}$. This results in a smoother sensitivity signal; the cost function serves as forcing to the adjoint model, and therefore needs to be smooth in both space and time. The cost function is therefore,

$$J = \sum_{i,j,k,n} W^{\text{space}}_{i,j,k} W^{\text{time}}_{n} T_{i,j,k,n} \tag{9}$$

$$W^{\text{space}}_{i,j,k} = \exp\left[-\left(\frac{x_i - x_{\max}}{\Delta X}\right)^2\right] \exp\left[-\left(\frac{y_j - y_{\max}}{\Delta Y}\right)^2\right] \times \exp\left[-\left(\frac{z_k - z_{\max}}{\Delta Z}\right)^2\right] \tag{10}$$

$$W^{\text{time}}_{n} = \exp\left[-\left(\frac{t_n - t_{\max}}{\Delta T}\right)^2\right], \tag{11}$$

where $x_{\max} = 100°\text{W}$, $y_{\max} = 0$, $z_{\max} = 60$ m is the location of maximum weight, $\Delta X = 3000$ km, $\Delta Y = 300$ km, $\Delta Z = 40$ m are scales similar to those of the model maximum temperature rms signal (Fig. 2), and x_i, y_j, z_k, t_n are the model coordinates. The connection between anomalies at the ocean surface and anomalies at the depth of the thermocline will be studied in section 7, using a modified cost function. Note that in sensitivity studies such as here, in contrast to cases where the adjoint model is used for calculating optimal initial conditions (Farrell 1988; Kleeman and Moore 1997; Penland and Sardeshmukh 1995), the cost function need not be quadratic and may be any function, linear or not, of the model state.

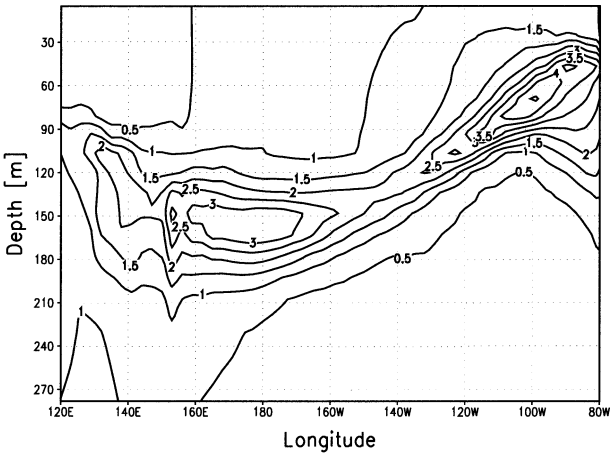

FIG. 2. Rms of the interannual variability of temperature in the model, averaged from 5°S to 5°N.

c. Choice of the control variables

The control variables $\mathbf{X}_{\text{init}}$ are all the initial prognostic variables, that is, temperature, salinity, currents, and surface height. In addition, one may examine the sensitivity to diagnostic and other intermediate model variables such as the wind stress, etc. that are also calculated by the adjoint model. Although the definition of the adjoint sensitivities (7) is straightforward, there are still some issues to consider when analyzing the results.

First, it is important to understand that the adjoint sensitivity reflects the effect of a perturbation in a specific place and time on the cost function. A high sensitivity does not mean that the actual probability for such a perturbation to occur is high. Second, one necessary measure to be taken before analyzing the adjoint solution is a normalization of all adjoint sensitivities by the volume of the model grid they represent. This compensates for the fact that the model grid is not uniform. A temperature perturbation in a deep grid box corresponds to a larger energy perturbation than the same temperature perturbation in a surface grid box, simply because the grid box size is larger at depth. The adjoint solution therefore biases the sensitivities toward the large-volume boxes, so that when analyzing the adjoint solution, this bias needs to be properly compensated for (Marotzke et al. 1999). All adjoint sensitivities appearing in this work are normalized by the volume of the box they represent, in such a way that the surface variables at the equator (smallest box volume) are normalized by a factor of 1. The normalization of the adjoint solution is done only when displaying and analyzing the results, and not during the adjoint model integration.

4. Sensitivities in the ocean-only model

In this section we study the adjoint sensitivities in an ocean-only model. This will set the stage for the in-

TABLE 1. List of sensitivity experiments.

Expt	Ocean–atmosphere coupling	t_{max}	Figures
Ocean-Dec	No	15 Dec	Figs. 3–4
Coupled-Dec	Yes*	15 Dec	Figs. 5–6
Ocean-Jun	No	15 Jun	Fig. 7
Coupled-Jun	Yes*	15 Jun	Fig. 8
Surface-Dec	No	15 Dec	Fig. 9
Surface-Jun	No	15 Jun	Fig. 10

* Statistical atmospheric model is set to perpetual Jan.

vestigation of the ocean–atmosphere coupling and its dependence on the seasonality of the thermocline outcropping in the later sections. For this purpose, we ran the coupled model with the coupling to the statistical atmosphere turned off, that is, the SST anomalies do not affect the winds and heat fluxes, and no interannual variability exists. These experiments therefore examine the free ocean dynamics. The forward model was run for one year (January to December) from its climatological state, so that the adjoint model is integrated backward in time for 1 yr with the model climatology as the background state; note that the model climatology will be used as the background state throughout the paper. The cost function (9) is calculated with t_{max} set to the middle of December, and the adjoint model is then run accordingly from December to January. This experiment will be referred to as ocean-December (Table 1).

Figure 3 shows the monthly averaged sensitivity of the cost function to temperature perturbations along the equator at 1, 3, 5, and 7 months prior to the time of the cost function evaluation. For reference we plot the 18° and 26° isotherms (which span the main thermocline temperature range) of the forward model climatology at the same months in which the sensitivities are displayed. The upper panel of Fig. 3 shows the sensitivity of the cost function, which is centered around December 15, to perturbations in the temperature field in November, that is, 1 month prior to the time of the cost function. These sensitivities indicate the relative effect on the cost function of temperature perturbations made at different locations during November. For example, we see from the figure that a temperature perturbation in November at a depth of 90 m at 120°W would be about 6 times more effective in changing the cost function 1 month later than the same perturbation applied to the temperature field at a depth of 90 m at the date line. The next panel shows the sensitivity of the same cost function to temperature perturbations in September, that is, 3 months prior to the time of cost evaluation.

The sensitivities are seen in Fig. 3 to propagate westward as an adjoint second baroclinic Kelvin wave (see section 3a earlier and van Oldenborgh et al. 1999; Philander 1990). The vertical structure of the sensitivity to perturbations in the zonal velocity (Fig. 4), with positive sensitivity above the thermocline, negative beneath it, and again positive sensitivity at larger depths (below the plotted depth range), reflects the vertical profile of the second baroclinic Kelvin wave. The adjoint Kelvin wave is seen to propagate from around 120°W in Fig. 4a, to around 160°E in Fig. 4b. Yet the sensitivity signal is not only due to the above adjoint Kelvin wave. Some of the sensitivity signal reaches the western boundary after 3 months, as expected from an equatorial adjoint Kelvin wave, but there is also a different sensitivity feature that is limited vertically to the thermocline depth range between 18° and 26°C, and which propagates much slower in time between 170° and 140°W. This feature may be a manifestation of some other physical processes, such as advection or higher baroclinic modes, yet it is not relevant to our main aim here.

The negative temperature sensitivity beneath the thermocline and positive sensitivity at and above the thermocline depth range appear in all sensitivity experiments presented here, and are simply a manifestation of the second baroclinic-mode structure of the sensitivity signal. The cost function in our model is sensitive to perturbations that have the vertical structure of the second baroclinic mode, hence the structure of the adjoint solution for the sensitivity. Note that both the positive and negative sensitivity signals are part of the same baroclinic structure that is of interest to us here. Higher baroclinic modes will clearly also consist of alternating positive and negative signals. Note also that the sign of the sensitivities in Fig. 3 depends on the formulation of the cost function. As the adjoint model is based on a tangent-linearization of the full model, the same cost function multiplied by -1 generates exactly the same sensitivities, but with an opposite sign.

The adjoint Kelvin wave temperature sensitivity signal is reflected as eastward-propagating, off-equatorial adjoint Rossby waves upon reaching the western boundary. These are not shown because our focus in this work is on the equatorial region and on a timescale of 1–7 months only. We now proceed to investigate the sensitivities in the coupled model.

5. Sensitivities in the coupled model

We ran the standard coupled model and its adjoint with t_{max} set again to the middle of December. The results of the coupled-model sensitivity experiment presented in this section are central to our objective. As explained in the introduction, the adjoint solution is a direct measure of the model's instability. An adjoint solution that grows backward in time indicates that the background state of the forward model is unstable to small perturbations. We expect to see such an instability in our model because our coupled model displays self-sustained variability. The self-sustained variability develops due to the fact that the seasonal background is unstable to small perturbations. If the forward coupled model were in a stable (damped) regime where small perturbations decay back to the seasonal background

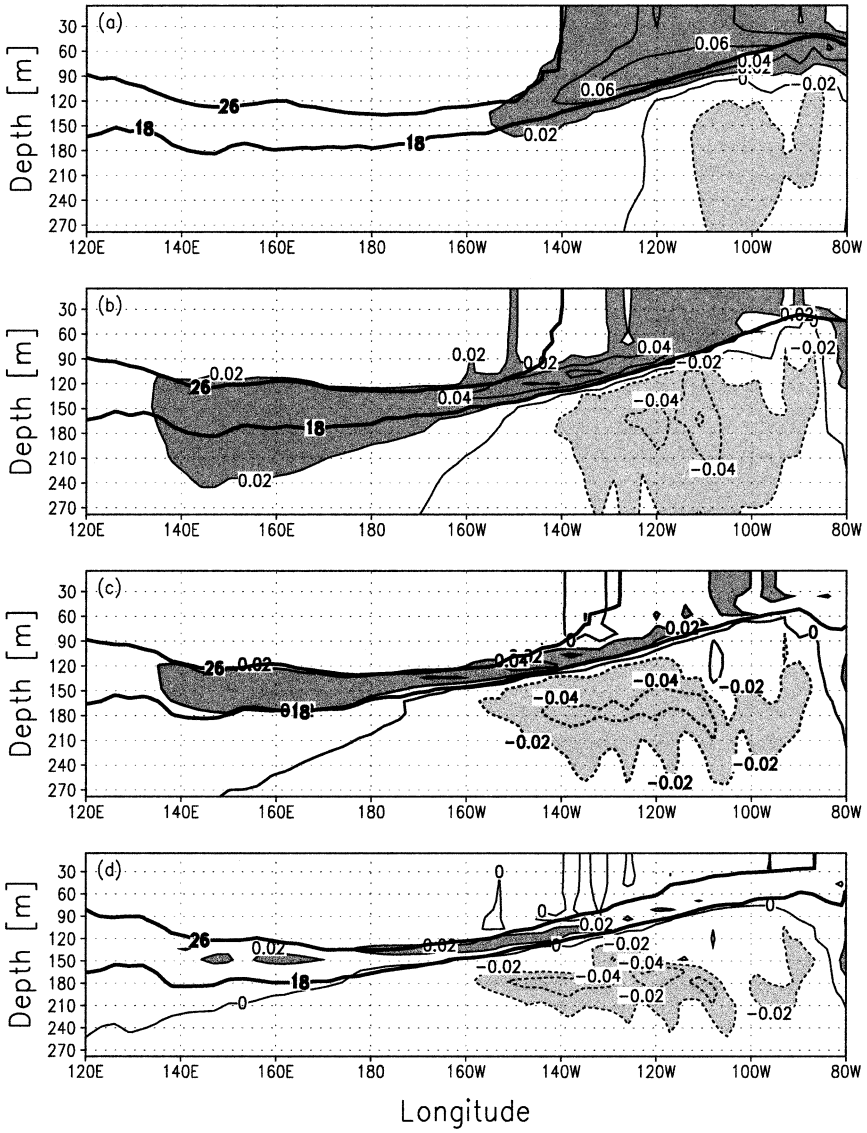

FIG. 3. The cost function sensitivity to temperature perturbations (units are dimensionless) along the equator in the ocean-Dec experiment, as a function of longitude and depth. The sensitivities are for (a) Nov, (b) Sep, (c) Jul, and (d) May, which are 1, 3, 5, and 7 months prior to the time of the cost function evaluation. Values larger (smaller) than 0.02 (−0.02) are shaded with dark (light) gray. For reference the 18° and 26°C isotherms are plotted.

state, then the adjoint solution would also be decaying backward in time.

The coupled model was run with the statistical atmospheric model set to perpetual January. This was done in order to isolate the effect of the thermocline outcropping on the seasonal instability strength, from the possible seasonal atmospheric influences. Figure 5 shows the sensitivity of the cost function to perturbations in the temperature field, as a function of longitude and depth, at different time intervals from the central time of the cost function evaluation, $t_{\max}$ (11). This experiment will be referred to as coupled-December (Table 1). It can be clearly seen that the sensitivity in the coupled model is much larger than in the ocean-December experiment. Furthermore, the sensitivities grow backward in time (that is, downward along the panels of Fig. 5) due to the amplification by the coupled ocean–atmosphere instability responsible for the self-sustained ENSO events in the forward model. The figure shows that the source of the sensitivity signal seems to be at the surface in the east Pacific, as anticipated from the coupled instability mechanism explained in the introduction. Once the sensitivities are amplified by the coupled ocean–atmosphere instability, they propagate in the ocean as in the ocean-December experiment.

We can now use the results of this experiment together

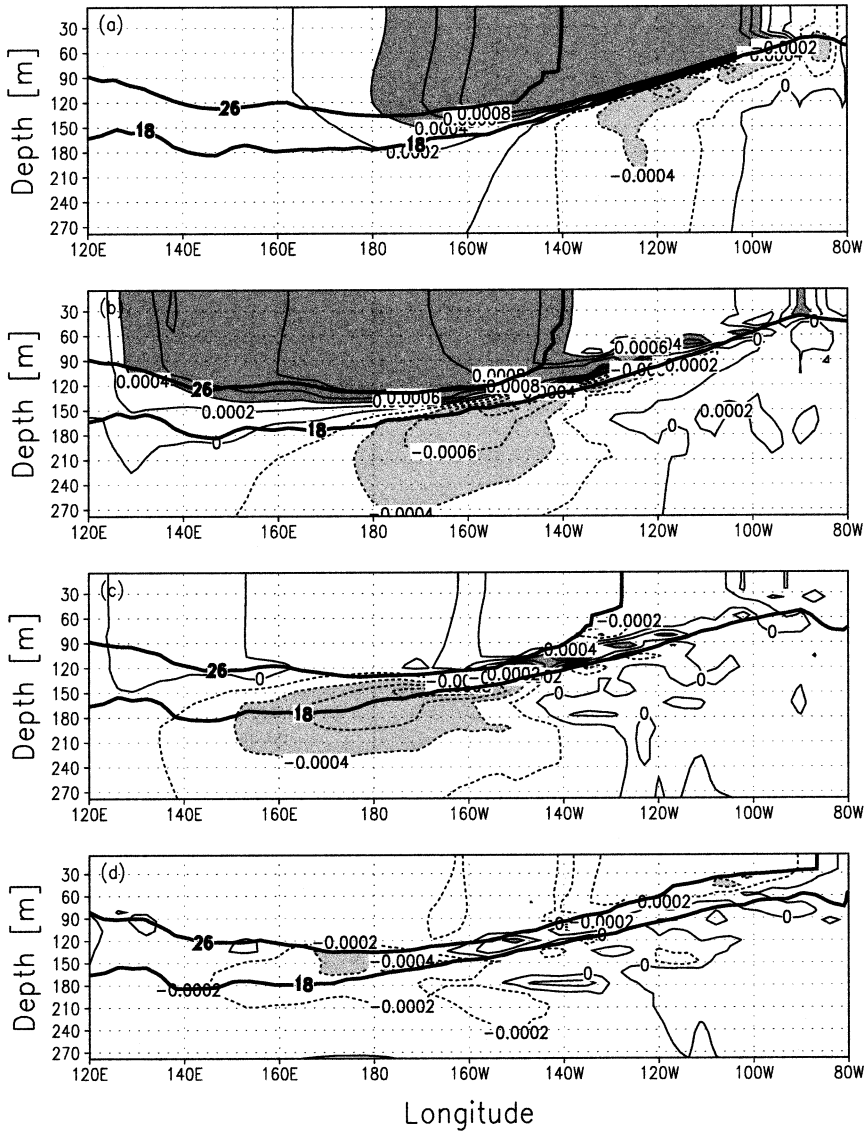

FIG. 4. Same as in Fig. 3 but for the sensitivity to the zonal velocity (units are °C m^{-1} s). Values larger (smaller) than 0.0004 (−0.0004) are shaded with dark (light) gray.

with those from section 4 to study the effect of the ocean–atmosphere coupling on the sensitivities. As the adjoint model is linear we can subtract the results of the ocean-December experiment from those of the coupled-December experiment (Fig. 6), thus isolating the role of the coupling. The growth of the sensitivities in time is especially evident in this plot. The timescale at which the coupled sensitivities grow is of the order of 6 months; at that time the sensitivities start to propagate westward along the thermocline. This timescale is partly a result of the timescale of the connection between the surface and the thermocline, which will be discussed in section 7.

The important lesson from this experiment is that the coupled ocean–atmosphere instability strongly amplifies the sensitivity of the east Pacific temperature evaluated at December to perturbation in previous months. We note at this stage that during the months July to December the thermocline, as indicated by the 18° and 26°C contours, outcrops over a wide region in the east Pacific, and we now examine the sensitivity of the east Pacific temperature evaluated during other months.

6. The thermocline outcropping and the seasonality of the coupled instability strength

So far we have analyzed the sensitivities of the averaged east Pacific temperature during December (i.e., the cost function was evaluated in December). In this section we finally get to the main point of this paper, and examine whether there are differences between sensitivities of our cost function when it is evaluated at

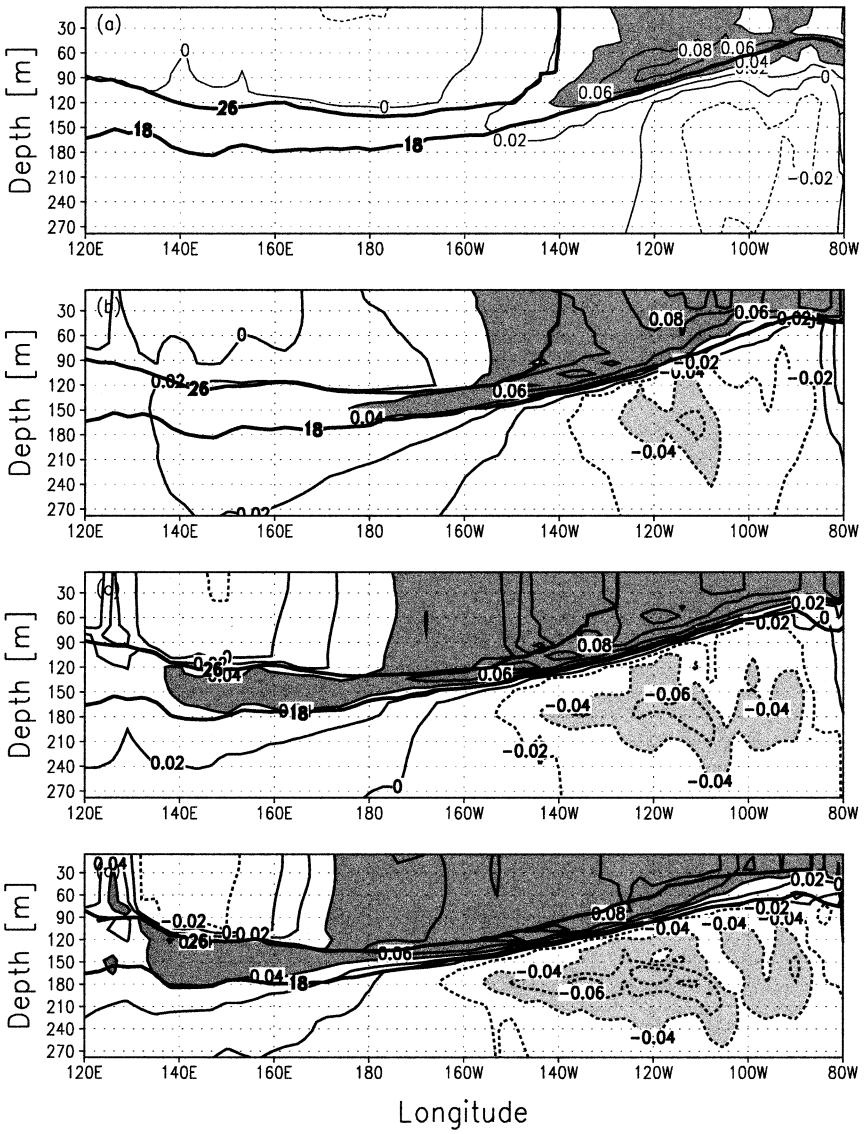

FIG. 5. Same as in Fig. 3 but for the coupled-Dec expt, where the coupled model was run with the statistical atmosphere set to perpetual Jan. Values larger (smaller) than 0.04 (−0.04) are shaded with dark (light) gray.

different times of the year. To address this issue we repeat the ocean-only and coupled-model sensitivity experiments of sections 4 and 5, with the cost function now centered in June rather than in December. The forward model is therefore run for 1 yr from July to June, and the adjoint model is run backward in time over the same period. These experiments will be referred to as ocean-June and coupled-June, respectively (Table 1). In the coupled-June experiment, the statistical atmospheric model is set to perpetual January, as was done in the coupled-December experiment earlier.

We first consider the ocean-only experiment (ocean-June; Fig. 7). In general, the evolution of the sensitivities is similar to those of the ocean-December experiment (Fig. 3), with some small differences in the dissipation rate and the propagation speed. The sensitivity to temperature perturbations in the ocean-December experiment is somewhat stronger than that in the ocean-June experiment during the first 3 months, yet the overall behavior is similar. The overall similarity between the ocean-December and the ocean-June experiments suggests that the propagation of perturbations within the subsurface water is only mildly influenced by the seasonal changes of the tropical Pacific ocean–atmosphere system. Thus, the pronounced seasonal behavior of the ocean–atmosphere instability strength must be a result of another characteristic of the system.

We now examine the coupled-June experiment. We use the fact that the adjoint sensitivity analysis is linear, and subtract the ocean-June results from the coupled-

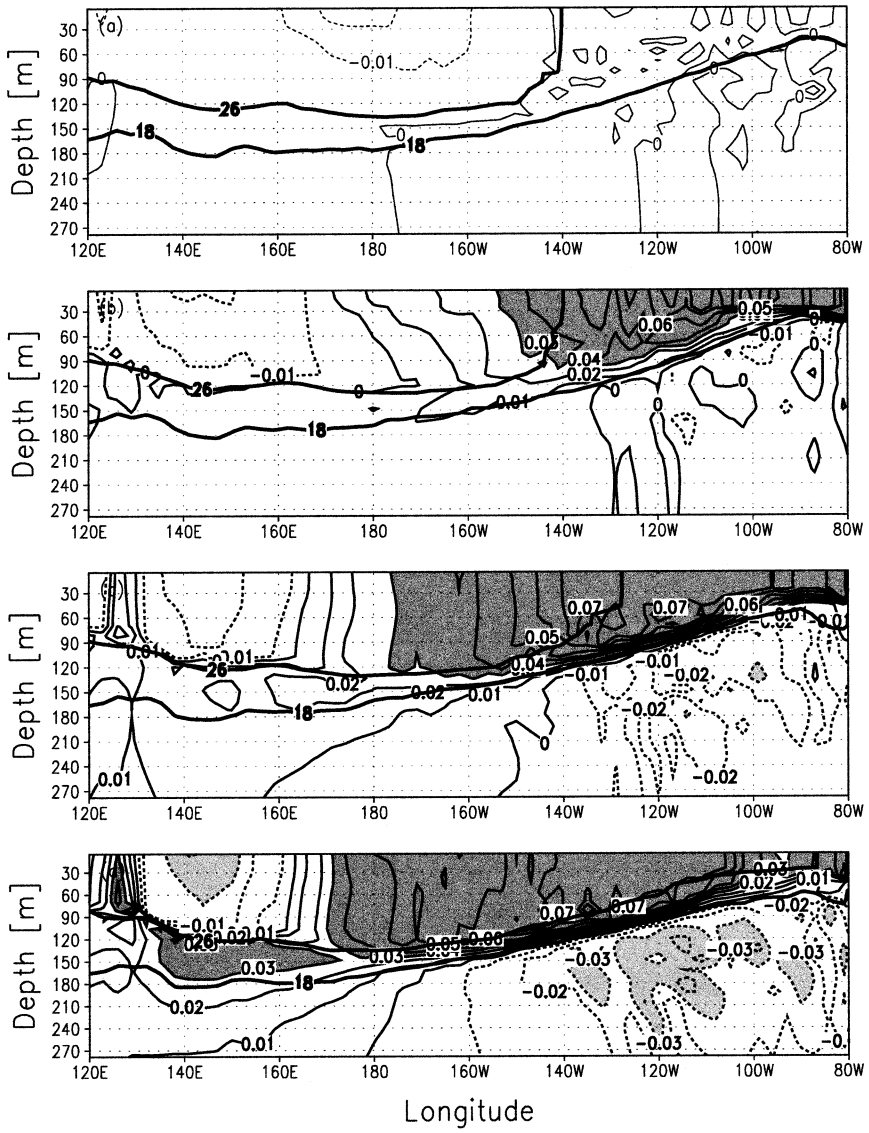

FIG. 6. Same as in Fig. 3 but for the difference between the coupled model (coupled-Dec expt) sensitivities and those of the ocean-only case (ocean-Dec expt). Values larger (smaller) than 0.03 (−0.03) are shaded with dark (light) gray. Note that the contour levels are different from those of Fig. 3.

June results to obtain the sensitivity due to the coupling only (Fig. 8). Comparing this experiment to the coupled-December experiment (Fig. 6) shows some significant differences. The sensitivities in the coupled-June experiment are weaker than those of the coupled-December experiment. Within the time interval of the 3 months prior to the cost evaluation, only minor differences can be seen, both in the sensitivity to temperature perturbations (cf. Figs. 8 and 6) and to zonal current perturbations (not shown). Pronounced differences appear in the time interval of 5 to 7 months, where the coupled-December experiment shows sensitivities that are 2 times stronger than the coupled-June experiment. For example, at 7 months prior to the cost evaluation, the sensitivity at 130°W at depth of 50 m is more than 0.07 in the coupled-December experiment, whereas in the coupled-June experiment it is about 0.03. The question, of course, is what causes this difference in sensitivities (which reflect difference in the coupled ocean–atmosphere instability strength) of the subsurface east Pacific temperature during December and June.

The main message of this paper is that the difference in the sensitivity between the December and June coupled sensitivity runs is a result of the outcropping location of the 26°C isotherm, or in other words, the instability strength is strongly influenced by the outcropping of the thermocline in the east Pacific. In the coupled-December experiment, the outcropping area of the

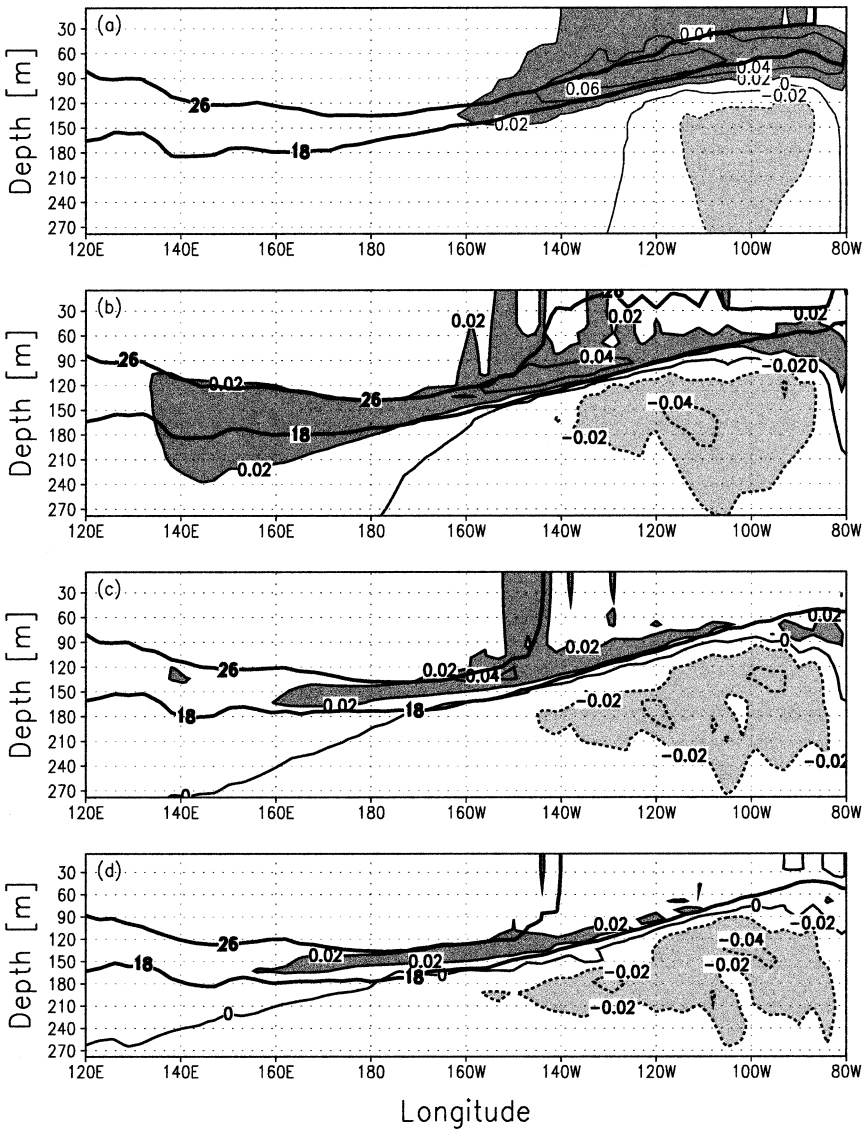

FIG. 7. The cost function (centered in Jun) sensitivity to temperature perturbations in the ocean-Jun expt, as a function of longitude and depth. The sensitivities are for (a) May, (b) Mar, (c) Jan, and (d) Dec, which are 1, 3, 5, and 7 months prior to the time of the cost function evaluation. Values larger (smaller) than 0.02 (−0.02) are shaded with dark (light) gray.

thermocline is initially very wide (the 26°C isotherm surfaces in December around 140°W so that the thermocline outcropping is from 140° to 80°W; Fig. 6a), enabling the subsurface temperature anomalies that propagate along the thermocline to reach the surface, affect the atmosphere, and be amplified by the coupled instability. In contrast, in the ocean-June experiment the outcropping area of the thermocline is initially very narrow (the 26°C isotherm surfaced in June only east of 70°W so that there is practically no outcropping; Fig. 8a), resulting in a very small area where the subsurface temperature anomalies can reach the surface. In other words, the warm surface water and strong upper-ocean stratification in the springtime decouples the surface from the thermocline, thus preventing sensitivities from entering the thermocline and propagating westward. Only in January are the surface temperature anomalies able to penetrate the mixed layer. As a result, the coupled sensitivities in the coupled-June experiment develop much later than those in the coupled-December experiment. The time window for the anomalies to develop is approximately from August to January, which is the time when the thermocline outcrops in the east Pacific.

The physical mechanism behind the difference between the adjoint sensitivities in the coupled-December case and those of the coupled-June case is the following: during the growth phase of ENSO, a warm (thermocline deepening) signal arrives in the east along the ther-

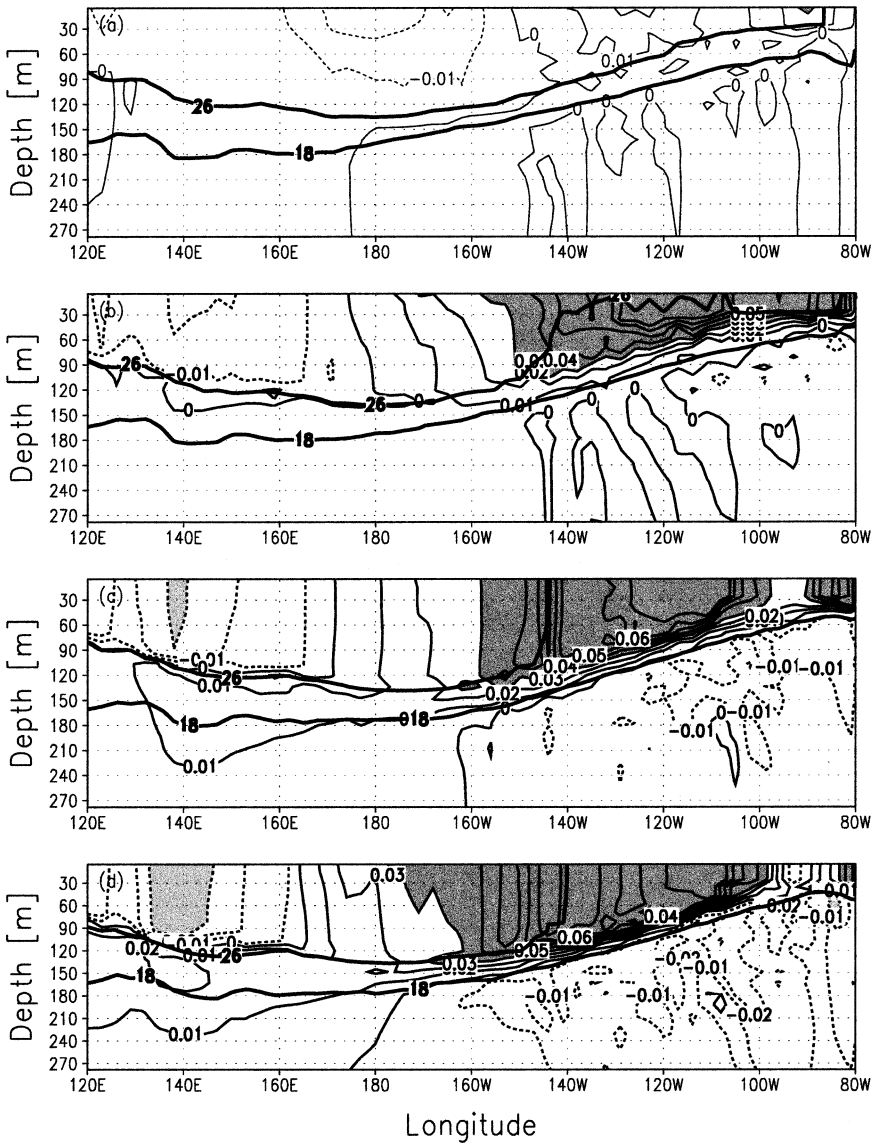

FIG. 8. Same as in Fig. 7, but for the difference between the coupled model (coupled-Jun expt) sensitivities and those of the ocean-only case (ocean-Jun expt). Contour levels are the same as in Fig. 6. Values larger (smaller) than 0.03 (−0.03) are shaded with dark (light) gray.

mocline. When the warm signal reaches the east, its degree of influence on the SST depends on the exposure of the thermocline at the surface; a thermocline-deepening signal that arrives in the east Pacific in springtime is decoupled from the surface due to the strong stratification between the surface and the thermocline; a warm signal that arrives in fall affects the surface substantially, as the thermocline is then exposed to the surface and any deepening of the thermocline immediately affects the heat balance of the surface water and hence the SST. This discussion could be extended to the different phases of ENSO as well, due to the different depth of the thermocline in the east Pacific at different ENSO phases. It has been shown by van Oldenborgh et al. (1999) that the sensitivities calculated over different climatologies (1987 and 1988) are very different. The difference in the climatology in their case was between an El Niño event and a La Niña event, yet the physical mechanism responsible for the difference may be similar to the one presented here: during the mature phase of an El Niño event the thermocline is buried deep under warm surface layers, and to a large extent is decoupled from the subsurface, whereas during the first stage of the event the surface is much more connected to the subsurface and therefore the event can grow.

The cost function we use is based on the temperature within the subsurface thermocline depth range, therefore at short time intervals (1–3 months) the thermocline

outcropping is not dominating the propagation of the sensitivities. However, at longer time intervals (more than 3 months), the coupling between the ocean and the atmosphere makes the thermocline outcropping a dominant factor in the ability of sensitivities to develop and be amplified. The sensitivities to perturbations in the subsurface temperature propagate westward where they create current sensitivities, which in turn create wind stress sensitivities. The wind stress sensitivities generate SST sensitivities in the east Pacific, and these penetrate to the thermocline as a function of the thermocline outcropping. We remind the reader that this ''adjoint'' scenario is the opposite of what happens in the forward model, where the SST anomalies excite the wind anomalies that in turn excite Kelvin waves that propagate eastward and affect the SST in the east Pacific; while the actual physical mechanism propagates from the *cause* to the *effect*, the sensitivities calculated by the adjoint model propagate from the *effect* to the *cause.*

7. The surface–thermocline connection

In order to clarify the role of the thermocline outcropping in determining the connection between the surface and the subsurface water, we conducted the following experiment: a cost function was set up to focus on the surface temperature at the equator at 120°W. We use the same cost function formulation of (9), but with $x_{\max} = 120°\text{W}$, $y_{\max} = 0$, $z_{\max} = 5$ m and $\Delta X = 500$ km, $\Delta Y = 200$ km, $\Delta Z = 1$ m. This spatial weighting puts the focus on the sea surface temperature along the equator at 120°W. The cost function time window was reduced to $\Delta T = 1$ day to enable shorter timescales to be resolved. The coupling to the statistical atmosphere was turned off so that all ocean–atmosphere coupling effects were excluded. This experiment will be referred to as surface-December (Table 1). Figure 9 shows the sensitivity of the cost function to temperature perturbations 15, 30, 45, and 60 days prior to the time of the cost function evaluation. At times of up to 1 month prior to the cost function evaluation time, the sensitivities remain within the region of the mixed layer, not able to penetrate the thermocline region. Only after about 45 days, do the sensitivities enter the thermocline depth range and propagate westward. The separation of the propagating feature (adjoint Kelvin wave) from other sensitivities, can be seen clearly after 30 days. The timescale of the surface to thermocline link is important to the ENSO dynamics and has been explored in detail by Jin and Neelin (1993) who studied the differences between the mixed-mode regime that includes the timescale of the surface to thermocline connection, and the fast SST regime that assumes an instantaneous adjustment of the SST to thermocline depth anomalies.

Next, we ran the same experiment but with the surface-centered cost function calculated in June (experiment surface-June; see Table 1, Fig. 10). The 26° isotherm now outcrops only at the eastern boundary, decoupling the surface from the thermocline. The sensitivities cannot penetrate the thermocline region and therefore are forced to remain in the mixed layer only. Some of the signal does propagate westward, thus creating a nonlocal sensitivity. But the propagation is above the thermocline depth range and not within it, indicating that the sensitivity is not due to the same baroclinic-mode wave propagation seen earlier. The sensitivity to the zonal velocity (not shown) is also weaker than in the surface-December experiment, indicating that the cost function in the surface-June experiment is less sensitive to Kelvin waves than the cost function in the surface-December experiment. This is a result of the inability of the sensitivities to penetrate the thermocline.

We now turn to the above two surface-centered sensitivity experiments after 5 months, in the warm pool area (Fig. 11). The difference is striking, the surface-December experiment shows sensitivities that are about 4 times larger than those of the surface-June experiment. The June sensitivities that concentrated above the thermocline at timescales of 1–2 months, dissipated due to the strong mixing within the mixed layer, while those of the surface-December experiment were able to propagate westward along the thermocline where mixing is much weaker.

Our assumption that the surface interacts with the thermocline mostly through the thermocline outcropping area implies that perturbations arriving in the east along the thermocline, will get to the surface by vertical mixing. When the thermocline outcrops over a wide area, the vertical stratification in the outcrop area is weak, and therefore mixing is strong. This means that a thermocline deepening signal arriving via a baroclinic Kelvin wave will be effective in reducing the mixing between the surface and the cold subsurface water, changing the heat balance of the surface water and causing a surface warming. On the other hand, when the thermocline does not outcrop, the vertical stratification is strong and the vertical mixing is already weak. A thermocline deepening signal arriving along the thermocline as a Kelvin wave will not reduce the already weak vertical mixing much more, and therefore will not have a large effect on the SST. We can use the adjoint method to test this assumption regarding the role of vertical mixing by running again the surface-December experiment, only this time with the terms in the adjoint model corresponding to vertical mixing shut off (experiment surface-December-no-mix; Table 1). Figure 12 shows the difference between the surface-December case and the case with no vertical mixing affecting the adjoint solution (experiment surface-December-no-mix). It is evident that in the no-vertical-mixing case, the surface sensitivities do not penetrate the thermocline, thus supporting our assumption that vertical mixing provides the link between the Kelvin waves propagating along the thermocline and the sea surface temperature.

These experiments support our hypothesis on the seasonal dependence of anomaly growth in the model. The outcropping of the thermocline in the east Pacific is what enables the Kelvin waves arriving in the east to influence

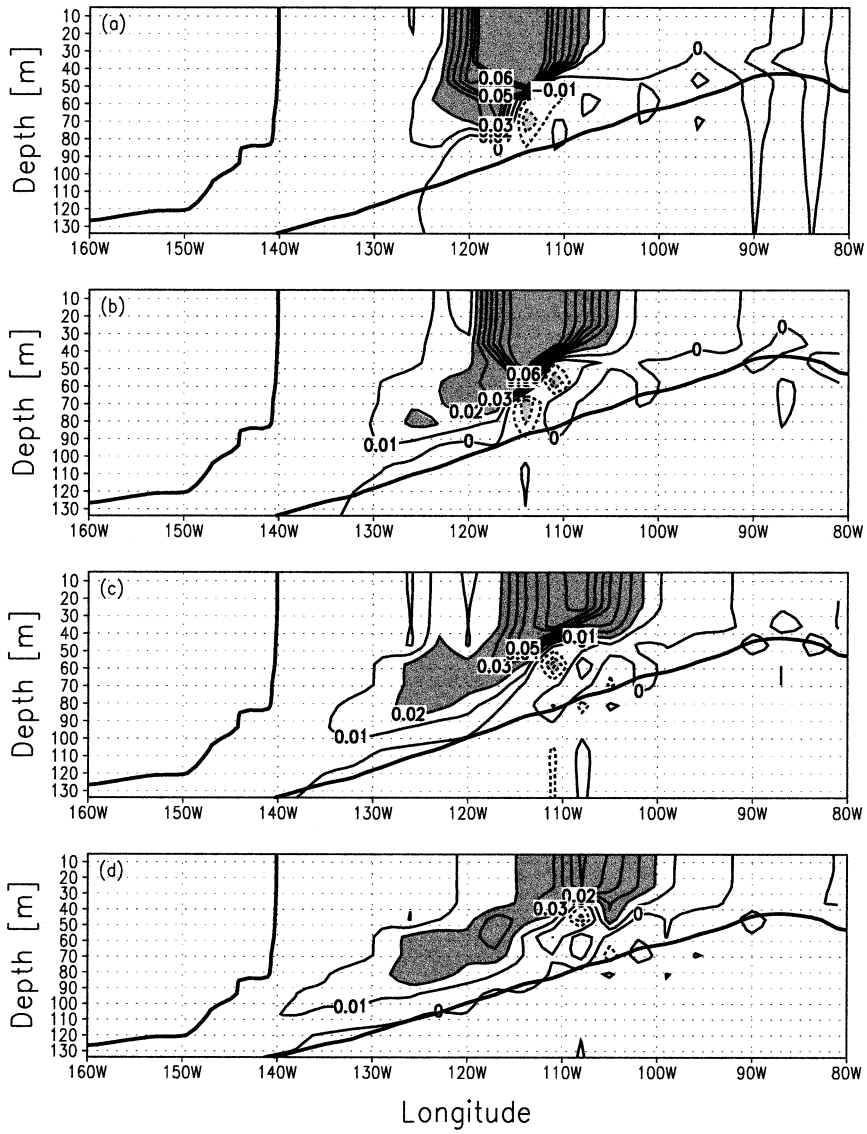

FIG. 9. Sensitivity of a cost function located at the surface and evaluated in Dec to temperature perturbations (a) 15, (b) 30, (c) 45, and (d) 60 days from the time of the cost function evaluation. Values larger (smaller) than 0.02 (−0.02) are shaded with dark (light) gray.

the SST. This outcropping occurs from summer to early winter, which is the time when ENSO grows the most. The formation of the strong stratification in the east Pacific in the later months of the winter prohibits the anomaly growth. This new insight is only possible because our ocean model explicitly resolves the thermocline and mixed layer. This mechanism is not represented in intermediate models that do not explicitly resolve the mixed layer dynamics or that do not include the seasonal variations in the thermocline depth (e.g., the CZ model).

Our focus here was the effect of the seasonal outcropping on the coupled ocean–atmosphere system dynamics. Accordingly, the background state used here for the adjoint model run and sensitivity analysis is the solution of the forward coupled model started from the ocean-only climatology. This solution is not far from the seasonal climatology of the ocean-only model. In principle, the adjoint sensitivity might change as function of the ENSO phase, as explored using the adjoint method by van Oldenborgh et al. (1999) or from a different perspective by Samelson and Tziperman (2001). This issue deserves further examination, yet is beyond the scope of the present work.

8. Discussion and conclusions

The problem of identifying a mechanism for the seasonal changes in the tropical Pacific ocean–atmosphere instability strength was addressed in many previous

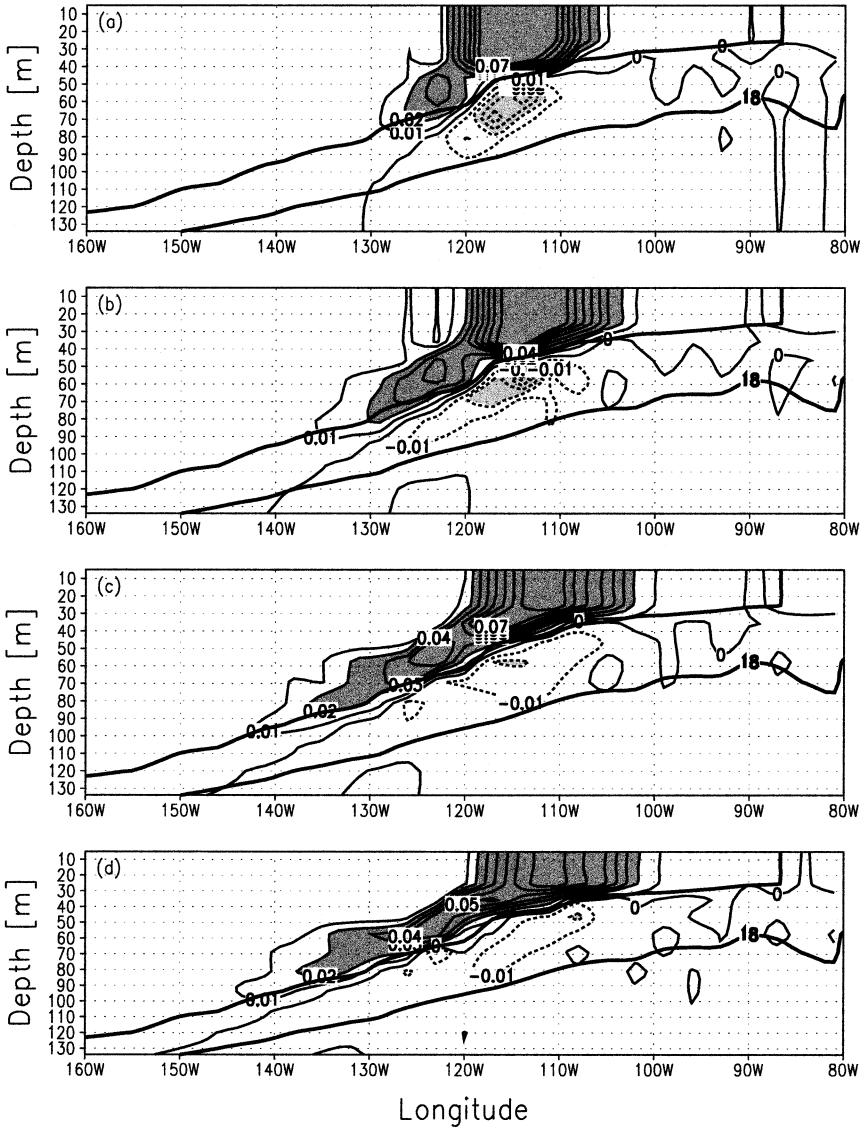

FIG. 10. Sensitivity of a cost function located at the surface and evaluated in Jun to temperature perturbations (a) 15, (b) 30, (c) 45, and (d) 60 days from the time of the cost function evaluation. Values larger (smaller) than 0.02 (−0.02) are shaded with dark (light) gray.

studies. However, most, if not all, of these previous works used simplified models, ranging from low-order models to intermediate models such as the Cane-Zebiak model (Zebiak and Cane 1987). Here we have used a hybrid coupled model, composed of an ocean GCM coupled to a statistical atmosphere, which allows us to examine physical processes not represented in intermediate models.

The positive feedback allowing the growth of anomalous conditions in the tropical Pacific can be described as follows: a positive SST perturbation in the east Pacific excites westerly wind anomalies in the central Pacific. These wind anomalies then excite downwelling Kelvin waves that propagate eastward. Upon reaching the east Pacific, the subsurface perturbations in the thermocline affect the sea surface temperature. The seasonality in the ocean–atmosphere coupling strength must, therefore, be due to a seasonal modulation in the effectiveness of one of the above processes.

Most of the simple and intermediate ENSO models represent the subsurface thermal structure of the equatorial Pacific by an upper warm layer and a deeper cold layer. The interaction between the surface and subsurface is commonly assumed to be a function of the movements of the thermocline separating the two layers. More specifically, the term that affects the SST in the CZ-like models is the advection by the upwelling that relates changes in SST to the thermocline depth. Vertical mixing is not explicitly included but is clearly implied in this parameterization via the way the upwelling af-

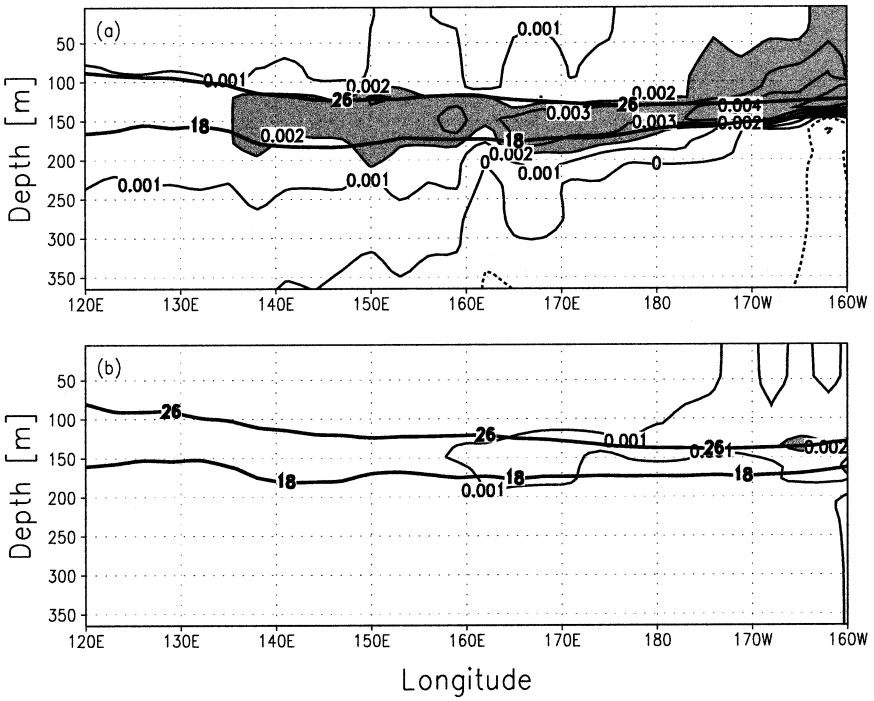

FIG. 11. Sensitivity of a cost function located at the surface to temperature perturbations, after 5 months: (a) Dec case and (b) Jun case. Values larger (smaller) than 0.002 (−0.002) are shaded with dark (light) gray.

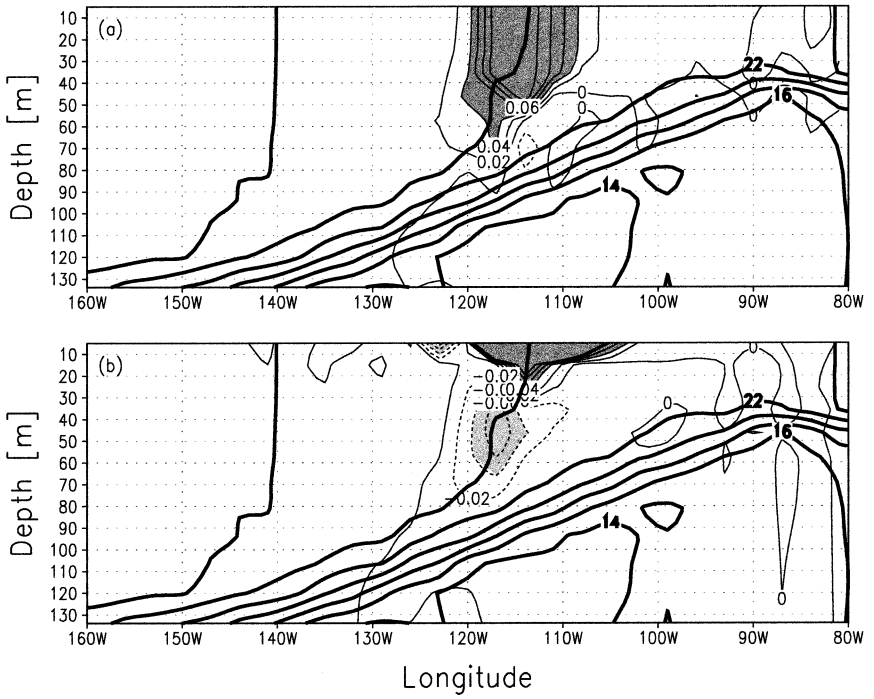

FIG. 12. The contribution of vertical mixing to the connection between the surface and the thermocline: (a) the temperature sensitivities after one month in the standard case, and (b) the sensitivities when the vertical mixing is shut off. Values larger (smaller) than 0.04 (−0.04) are shaded with dark (light) gray.

fects the SST if the thermocline nears the surface. While having the advantage of simplicity, these models do not include the seasonal movements of the thermocline and its outcropping, and they also lack the explicit effect of this vertical thermocline movement on the vertical mixing between the surface and the subsurface waters.

In this work we showed that an important factor determining the strength of the coupled ocean–atmosphere instability and its seasonal variations is the strength of the east Pacific SST response to changes in the thermal structure beneath it. We found that the outcropping of the thermocline in the east equatorial Pacific controls the SST response to subsurface temperature anomalies. When a warm thermocline deepening signal reaches the east Pacific as downwelling Kelvin waves, its influence on the surface (sea surface temperature) depends on the exposure of the thermocline at the surface; a thermocline deepening signal that arrives in late winter to springtime, when there is a strong stratification and therefore weak vertical mixing between the thermocline and the surface, will not affect the vertical mixing and will therefore not affect the SST. On the other hand, a warm thermocline deepening signal that arrives in fall and early winter, when the thermocline is then exposed to the surface, the stratification is weak and vertical mixing between the thermocline and the surface is strong, will be able to weaken the mixing between the cold subsurface water and the surface water, and induce an SST warming. The seasonal ocean–atmosphere coupling strength is therefore influenced by the seasonal changes in the east Pacific thermocline outcropping.

The modulation of the subsurface to surface connection by the seasonal changes in the thermocline outcropping is relevant also to the effect of vertical thermocline movements through the ENSO cycle. Our discussion of the role of thermocline outcropping and vertical mixing may therefore also be relevant to the analysis of van Oldenborgh et al. (1999), which found changes in ENSO's sensitivity during different phases of the ENSO cycle.

Neelin et al. (2000) showed that changing the mixed layer parameterization in their model, shifted the peak of the model ENSO events by a few months, although they could not explain this in terms of a specific physical mechanism. A wave dynamics mechanism for ENSO's phase locking was presented by Tziperman et al. (1998) and Galanti and Tziperman (2000). This mechanism is based on the seasonal variations of the ocean–atmosphere instability strength that affects the amplification of ocean waves. The present work shows that the coupled instability strength and its seasonal variations are strongly affected by the mixed layer processes through the thermocline outcropping dynamics. We therefore suggest here that the mixed layer parameterization affects the coupled instability strength and its seasonal variations (via the thermocline outcropping mechanism). Therefore the mixed layer parameterization affects the seasonal amplification of ocean waves, and may influence the phase locking of ENSO as observed by Neelin et al. (2000), based on the dynamical explanations of Tziperman et al. (1998) and Galanti and Tziperman (2000).

The study of the thermocline outcropping and its effect on the instability strength was made possible thanks to the use of a full 3D ocean model. It would be interesting to further examine the issue using higher-resolution models with improved representation of mixed layer processes.

Acknowledgments. This work was partially funded by the Israeli Science Foundation, and by NOAA through the office of global programs. We are grateful to Ron Pacanowski for making the version of MOM used here available to us, and to Andrew Moore and Geert Jan van Oldenborgh for their most constructive and useful reviews.

REFERENCES

Battisti, D. S., 1988: The dynamics and thermodynamics of a warming event in a coupled tropical atmosphere/ocean model. *J. Atmos. Sci.,* **45,** 2889–2919.

——, and A. C. Hirst, 1989: Interannual variability in the tropical atmosphere–ocean model: Influence of the basic state, ocean geometry, and nonlinearity. *J. Atmos. Sci.,* **46,** 1687–1712.

Cane, M. A., M. Munnich, and S. E. Zebiak, 1990: A study of self-excited oscillations of the tropical ocean–atmosphere system. Part I: Linear analysis. *J. Atmos. Sci.,* **47,** 1562–1577.

Chang, P., B. Wang, T. Li, and L. Ji, 1994: Interactions between the seasonal cycle and the Southern Oscillation—Frequency entrainment and chaos in a coupled ocean–atmosphere model. *Geophys. Res. Lett.,* **21,** 2817–2820.

Chen, D., S. E. Zebiak, A. J. Busalacchi, and M. A. Cane, 1995: An improved procedure for El Niño forecasting: Implications for predictability. *Science,* **269,** 1699–1702.

Errico, R. M., and T. Vukicevic, 1992: Sensitivity analysis using an adjoint of the PSU–NCAR Mesoscale Model. *Mon. Wea. Rev.,* **120,** 1644–1660.

Esbensen, S. K., and V. Kushnir, 1981: The heat budget of the global ocean: An atlas based on estimates from surface marine observations. Tech. Rep. 29, Climate Research Institute Oregon State University, Corvallis, OR, 27 pp.

Farrell, B., 1988: Optimal excitation of neutral Rossby waves. *J. Atmos. Sci.,* **45,** 163–172.

Galanti, E., and E. Tziperman, 2000: ENSO's phase locking to the seasonal cycle in the fast SST, fast wave, and mixed mode regimes. *J. Atmos. Sci.,* **57,** 2936–2950.

Gibson, J., S. Kallberg, S. Uppala, A. Nomura, A. Hernandez, and E. Serrano, 1997: ECMWF reanalysis project report series no. 1. Tech. Rep. 1, ECMWF, Shinfield Park, Reading, United Kingdom, 71 pp.

Giering, R., 1997: TAMC: Tangent linear and adjoint model compiler, users manual. [Available online at http://www.autodiff.com/tamc/.]

——, and T. Kaminski, 1998: Recipes for adjoint code construction. *ACM Trans. Math. Software,* **24,** 437–474.

Gu, D., and S. G. H. Philander, 1995: Secular changes of annual and interannual variability in the Tropics during the past century. *J. Climate,* **8,** 864–876.

——, and ——, 1997: Interdecadal climate fluctuations that depend on exchanges between the tropics and extratropics. *Science,* **275,** 805–807.

Hall, M. C. G., 1986: Application of adjoint sensitivity theory to an atmospheric general circulation model. *J. Atmos. Sci.,* **43,** 2644–2651.

Harrison, M., E. Galanti, A. Rosati, B. J. Soden, and E. Tziperman, 2002: An examination of air–sea flux products for ENSO simulation and prediction. *Mon. Wea. Rev.,* **130,** 723–732.

Hirst, A. C., 1986: Unstable and damped equatorial modes in simple coupled ocean–atmosphere models. *J. Atmos. Sci.,* **43,** 606–630.

Jin, F.-F., and D. Neelin, 1993: Models of interannual tropical ocean–atmosphere interaction—A unified view. Part I: Numerical results. *J. Atmos. Sci.,* **50,** 3477–3503.

——, ——, and M. Ghil, 1994: ENSO on the devil's staircase. *Science,* **264,** 70–72.

Kleeman, R., and A. M. Moore, 1997: A theory for the limitation of ENSO predictability due to stochastic atmospheric transients. *J. Atmos. Sci.,* **54,** 753–767.

Levitus, S. E., 1982: *Climatological Atlas of the World Ocean.* NOAA Prof. Paper 13, 173 pp. and 17 microfiche.

Marotzke, J., R. Giering, K. Q. Zhang, D. Stammer, C. Hill, and T. Lee, 1999: Construction of the adjoint MIT ocean general circulation model and application to Atlantic heat transport sensitivity. *J. Geophys. Res.,* **104,** 29 529–29 547.

Moore, A. M., and R. Kleeman, 1996: The dynamics of error growth and predictability in a coupled model of ENSO. *Quart. J. Roy. Meteor. Soc.,* **122,** 1405–1446.

——, and ——, 1997: The singular vectors of a coupled ocean–atmosphere model of ENSO. II: Sensitivity studies and dynamical interpretation. *Quart. J. Roy. Meteor. Soc.,* **123,** 983–1006.

Neelin, J., F. Jin, and H. Syu, 2000: Variations in ENSO phase locking. *J. Climate,* **13,** 2570–2590.

Pacanowski, R. C., and S. G. H. Philander, 1981: Parameterization of vertical mixing in numerical models of tropical oceans. *J. Phys. Oceanogr.,* **11,** 1443–1451.

——, and S. M. Griffies, 1999: MOM 3.0 Manual. NOAA/Geophysical Fluid Dynamics Laboratory, Princeton, NJ, 671 pp.

Penland, C., and P. D. Sardeshmukh, 1995: The optimal growth of tropical sea surface temperature anomalies. *J. Climate,* **8,** 1999–2024.

Philander, S. G., 1983: El Niño Southern Oscillation phenomena. *Nature,* **302,** 295–301.

——, 1990: *El Niño, La Niña, and the Southern Oscillation.* Academic Press, 293 pp.

Reynolds, R. W., and T. M. Smith, 1994: Improved global sea surface temperature analyses using optimum interpolation. *J. Climate,* **7,** 929–948.

Samelson, R., and E. Tziperman, 2001: Predictability of the chaotic ENSO: The growth phase predictability barrier. *J. Atmos. Sci.,* **58,** 3613–3625.

Sirkes, Z., and E. Tziperman, 2001: Identifying a damped oscillatory thermohaline mode in a general circulation model using an adjoint model. *J. Phys. Oceanogr.,* **31,** 2297–2306.

Stricherz, J. J. O., and D. M. Legler, 1992: Atlas of Florida State University tropical Pacific winds for TOGA 1966–1985. Florida State University, Tallahassee, FL, 275 pp.

——, ——, and J. J. O'Brien; 1997: *Indian Ocean.* Vol. 3, *TOGA Pseudostress Atlas 1985–1994,* Florida State University, Tallahassee, FL, 155 pp.

Syu, H., and J. Neelin, 2000: ENSO in a hybrid coupled model. Part I: Sensitivity to physical parameterizations. *Climate Dyn.,* **16,** 19–34.

——, ——, and D. Gutzler, 1995: Seasonal and interannual variability in a hybrid coupled GCM. *J. Climate,* **8,** 2121–2143.

Thacker, W. C., 1987: Three lectures on fitting numerical models to observations. External Rep. GKSS 87/e/65, GKSS-Forschungszentrum Geesthacht GmbH, Geesthacht, Germany, 64 pp.

Torrence, C., and P. J. Webster, 1998: The annual cycle of persistence in the El Niño Southern Oscillation. *Quart. J. Roy. Meteor. Soc.,* **124,** 1985–2004.

Tziperman, E., and W. C. Thacker, 1989: An optimal-control/adjoint-equations approach to studying the oceanic general circulation. *J. Phys. Oceanogr.,* **19,** 1471–1485.

——, L. Stone, M. A. Cane, and H. Jarosh, 1994: El-Nino chaos: Overlapping of resonances between the seasonal cycle and the Pacific ocean–atmosphere oscillator. *Science,* **264,** 72–74.

——, M. A. Cane, and S. E. Zebiak, 1995: Irregularity and locking to the seasonal cycle in an ENSO prediction model as explained by the quasi-periodicity route to chaos. *J. Atmos. Sci.,* **52,** 293–306.

——, S. E. Zebiak, and M. A. Cane, 1997: Mechanisms of seasonal–ENSO interaction. *J. Atmos. Sci.,* **54,** 61–71.

——, M. A. Cane, S. E. Zebiak, Y. Xue, and B. Blumenthal, 1998: Locking of El Niño's peak time to the end of the calendar year in the delayed oscillator picture of ENSO. *J. Climate,* **11,** 2191–2199.

van Oldenborgh, G., 2000: What caused the onset of the 1997/98 El Niño? *Mon. Wea. Rev.,* **128,** 2601–2607.

——, G. Burgers, S. Venzke, C. Eckert, and R. Giering, 1999: Tracking down the ENSO delayed oscillator with an adjoint OGCM. *Mon. Wea. Rev.,* **127,** 1477–1495.

Webster, P. J., and S. Yang, 1992: Monsoon and ENSO: Selectively interactive systems. *Quart. J. Roy. Meteor. Soc.,* **118,** 877–926.

Weiss, J. P., and J. B. Weiss, 1999: Quantifying persistence in ENSO. *J. Atmos. Sci.,* **56,** 2737–2760.

Xue, Y., M. A. Cane, S. E. Zebiak, and M. B. Blumenthal, 1994: On the prediction of ENSO: A study with a low order Markov model. *Tellus,* **46A,** 512–528.

Zebiak, S. E., and M. A. Cane, 1987: A model El Niño–Southern Oscillation. *Mon. Wea. Rev.,* **115,** 2262–2278.